This is a repository copy of *The synergetic effects of shot peening and laser-shot peening on the microstructural evolution and fatigue performance of a medium carbon steel*.

White Rose Research Online URL for this paper:
https://eprints.whiterose.ac.uk/190904/

Version: Accepted Version

Article:
Zhang, Y., Zhang, K., Hu, Z. et al. (3 more authors) (2023) The synergetic effects of shot peening and laser-shot peening on the microstructural evolution and fatigue performance of a medium carbon steel. International Journal of Fatigue, 166. 107246. ISSN 0142-1123

https://doi.org/10.1016/j.ijfatigue.2022.107246

© 2022 Published by Elsevier Ltd. This is an author produced version of a paper subsequently published in International Journal of Fatigue. Uploaded in accordance with the publisher's self-archiving policy. Article available under the terms of the CC-BY-NC-ND licence (https://creativecommons.org/licenses/by-nc-nd/4.0/).

Reuse
This article is distributed under the terms of the Creative Commons Attribution-NonCommercial-NoDerivs (CC BY-NC-ND) licence. This licence only allows you to download this work and share it with others as long as you credit the authors, but you can't change the article in any way or use it commercially. More information and the full terms of the licence here: https://creativecommons.org/licenses/

Takedown
If you consider content in White Rose Research Online to be in breach of UK law, please notify us by emailing eprints@whiterose.ac.uk including the URL of the record and the reason for the withdrawal request.

eprints@whiterose.ac.uk
https://eprints.whiterose.ac.uk/

The synergetic effects of shot peening and laser-shot peening on the microstructural evolution and fatigue performance of a medium carbon steel

Yating Zhang[1,2], Kun Zhang [1,2,*], Zheng Hu [3], Tianyu Chen[1], Luca Susmel[4], Bingchen Wei [1,2,*]

[1]Key Laboratory of Microgravity (National Microgravity Laboratory), Institute of Mechanics, Chinese Academy of Sciences, Beijing 100190, China

[2]School of Engineering Science, University of Chinese Academy of Sciences, Beijing 100049, China

[3]Science and Technology on Vehicle Transmission Laboratory, China North Vehicle Research Institute, Beijing, 100072, China

[4] Department of Civil and Structural Engineering, The University of Sheffield, Sheffield, S1 3JD, UK

Email: zhangkun@imech.ac.cn; weibc@imech.ac.cn

Abstract

The synergetic effect of shot peening (SP) and laser shot peening (LSP) on the fatigue behavior of a medium carbon steel was investigated. A fatigue life transition was observed in the S-N curve, where the fatigue performance of the SP + LSP specimen was improved only at lower stress levels. This result is consistent with the short crack propagation behavior observed in the near-threshold region. The heterogeneous structures comprised by ultra-fine grains, dislocation tangles, and more high-angle grain boundaries were responsible for this behavior which effectively retard the short crack propagation.

Keywords: Shot peening; Laser shot peening; Fatigue life transition; Microstructure; Short crack.

*Corresponding Author

Email addresses: zhangkun@imech.ac.cn
weibc@imech.ac.cn

Nomenclature

T	The stress-based scatter index	$\dot{\gamma}_0$	the reference shearing rate
K	Negative inverse slope of the Wohler curve	M	Taylor factor
Ra	She arithmetic average height	η	Material constant
σ^2	The variance of roughness	N_d	the total number of the piling-up dislocations
α	Material constant	μ	The shear modulus of matrix
d	Grain size	ν	Poisson's ratio
$\Delta\varepsilon_p$	Macroscopic plastic strain range	b	Burger vector
$N_{incubation}$	The crack incubation life	θ	The angle of misorientation between HAGBs
τ_{eff}	The efficient resolved shear stress	d_t	The distance of dislocation tangle and cells
τ	The resolved shear stress	τ_p	The kinematic back stress caused by cementite particles
τ_b	The kinematic back stress	φ	Material constant
$\dot{\gamma}$	The plastic slip rate	D	The distance of the strong microstructural barrier
m	Material constant	a	The crack length
σ_r	The slip resistance	Δt	The time interval
k_{th}	Hall-petch slope	f	Loading frequency

Abbreviations

CRS	Compressive residual stress	EBSD	Electron backscatter diffraction
FCG	Fatigue crack growth	TEM	Transmission electron microscope
FWHM	Full width at half maxima	XRD	X-ray diffraction
PS	Possible of survival	HCF	High cycle fatigue
LCF	Low cycle fatigue	IPF	Inverse pole figure
HAGB	High angle grain boundary	SEM	Scanning electron microscope

1. Introduction

Fatigue failure is one of the most detrimental forms of failure displayed by in-service materials and structures. Generally, fatigue breakage is characterized by three distinct phases: crack initiation, crack propagation, and sudden final failure. Fatigue damage is governed by irreversible plastic flow under cyclic loads [1]. In most polycrystalline alloys damaged by fatigue, cyclic slip is the primary mechanism and is the result of dislocation motion [1-3]. As fatigue microstrain accumulates on the surface or subsurface of materials, plastic deformation localizes to develop short cracks, which grow into long cracks and eventually lead to fatigue failure [4]. Many studies [1, 5, 6] have shown that irreversible slip is the result of dislocation motion, including annihilation, cross-slipping, penetrating precipitates, transmission through grain boundaries, and piling-up. The microstructure plays a significant role in determining the mean free path of dislocations and the associated efficient resolved shear stress on each slip system [7, 8]. Therefore, proper mechanical surface treatments that alter the surface morphologies and introduce gradient structures on the surface and subsurface can inhibit short crack initiation and propagation in the microstructure [9-13]. Short cracks can be arrested to retard fatigue crack propagation and increase the fatigue life. Conventionally, these mechanical surface treatments include shot peening (SP) [10, 14], laser shot peening (LSP) [15, 16], deep rolling [17], and cold expansion [18].

SP is an effective surface strengthening treatment that has been widely employed to improve the mechanical properties and fatigue behavior of metallic materials. It introduces compressive residual stress (CRS) and modifies microstructures through plastic deformation to delay the microstructural short crack initiation [19, 20]. The strengthening effects of SP treatment depend on grain refinement and a higher dislocation density due to the impact indentation of the shots. However, SP treatment increases the surface roughness and generates microcracks, which limits the enhancement of the fatigue

performance [10, 21]. In contrast to SP, LSP uses high-magnitude and transient shock waves that generate a deeper CRS layer but with decreased surface roughness, which provides better fatigue performance [22]. The deformation mechanism and the associated strengthening mechanism of LSP with a high strain rate (usually 10^6 s^{-1}) are different from those of SP. For instance, for Ti-6Al-4V [9, 23], LSP with high-density dislocations produced more directional planar dislocations, dislocation network cells, subgrains, and more high-angle grain boundaries (HAGBs). In contrast, SP generated long wavy tangled dislocation structures and significant shear deformation. However, residual stress holes have been observed in some metallic materials surface-treated with LSP [24, 25], which destroy the uniformity of the CRS distribution on the surface and provide inhomogeneous work hardening that restricts improvements in the fatigue life.

It is unclear whether SP and LSP can be applied together to synergistically incorporate their individual advantages. Recently, Luo et al. [9] investigated the fatigue performance of Ti-6Al-4V by sequential LSP and SP surface treatment, and they found that the fatigue life of specimens subjected to LSP+SP treatment was 3.54 and 1.98 times higher than those with SP and LSP treatments alone, respectively. They attributed this enhancement to the deeper CRS layer, as well as a plastically-hardened surface layer. Still, a higher roughness was observed for the specimens with the LSP+SP treatment, which may cause undesirable notches that act as potential crack initiation sites. Therefore, to inhibit this, the treatments can be applied in the reverse order.

It seems that combining SP and LSP is an effective approach to increase the fatigue life, but microstructural evolution and its relation to the macro-mechanical properties have not yet been fully investigated [26, 27]. The aim of this paper is to investigate the microstructural evolution and fatigue macro-mechanical property enhancement after surface treatment combining SP and LSP. To this end, a typical medium carbon steel (quenched and tempered 30CrMnSiA) subjected to SP+LSP treatment was

studied and compared to a baseline specimen with SP treatment alone. The fatigue performance of 30CrMnSiA after two surface treatments, SP+LSP and SP alone, was assessed through S-N curves generated by fatigue tests, as well as the surface roughness examinations as the notch effect. The microstructure evolution was investigated by electron backscatter diffraction (EBSD) and transmission electron microscopy (TEM) and then related to macro-mechanical fatigue performance improvements.

2. Experimental

2.1 Specimen preparation

To study the synergetic effects of the combination of SP and LSP treatments, a typical medium carbon steel (quenched and tempered 30CrMnSiA) subjected to SP+LSP surface treatments were prepared with SP specimens as a baseline comparison. The grain size of such medium carbon steel is about 20 μm, in which the microstructures are considered as the white cementite particles with dozens of nanometers distributed in the black ferrite matrix as shown in Fig. A.1. The chemical composition in weight percent is provided in Table 1. The yield strength, ultimate strength and fracture strain during tensile test are 960 MPa, 1053 MPa and 16.5% as shown in Fig. 1, respectively.

For the SP treatment (Fig. 2(a)), the front and back surfaces of S-N fatigue and FCG specimens were both treated. The detailed SP parameters are as follow: the S70 cast steel shot media with a diameter of 0.17 mm; the Almen intensity is 0.202 A; the peening duration is about 20 s; the pressure in air compressor is about 0.38 MPa; and the peening impact angle is 90°. In order to prevent the corner from being severely deformed [28], the un-peened sides of the S-N fatigue specimens are glued with rubber protective tooling during SP treatment and then slightly polished. Moreover, this method has been widely used for investigating the relationship between the reshaped subsurface microstructures after surface

treatment and their fatigue behavior [16, 29-32]. These specimens are denoted as SP specimens.

For the SP+LSP treatments (Fig. 2(b)), the SP specimens were further treated by the LSP process. The LSP treatment was carried out by a Q-switched Nd: YAG pulse laser with 1064 nm wavelength (pulse duration: 30 ns, maximum pulse energy: 1.6 J). The aluminum foil (~30 μm) was chosen as the ablative coating layer, and purified water was chosen as the confining medium. During the LSP, the size of the spot is about 2 mm, the scanning pitch is about 1 mm (an overlap rate of 50%). In addition, the un-peened sisde of these specimens are treated as the same with that in the SP specimens, that is, protected by rubber tooling.These specimens are denoted as SP+LSP specimens.

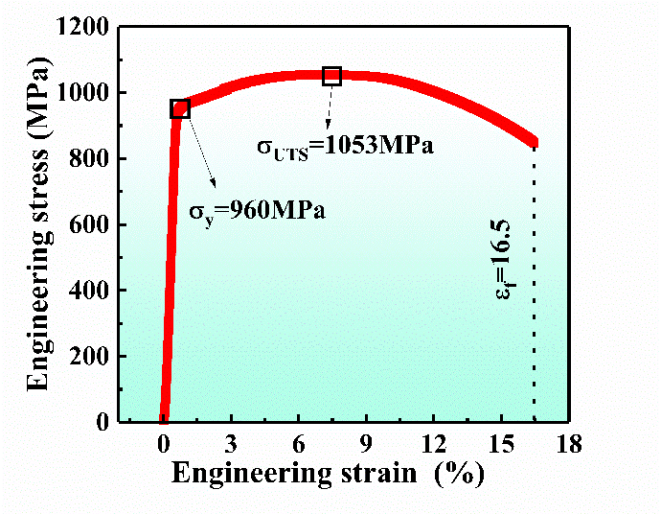

Fig. 1. The tensile stress-strain curve of 30CrMnSiA steel.

Table 1. The chemical composition of 30CrMnSiA (wt%)

C	Si	Mn	P	S	Cr	Mo	Ti	V	W	Cu	Ni
0.305	1.08	1.00	0.017	0.003	0.99	0.001	0.004	0.007	0.002	0.013	0.012

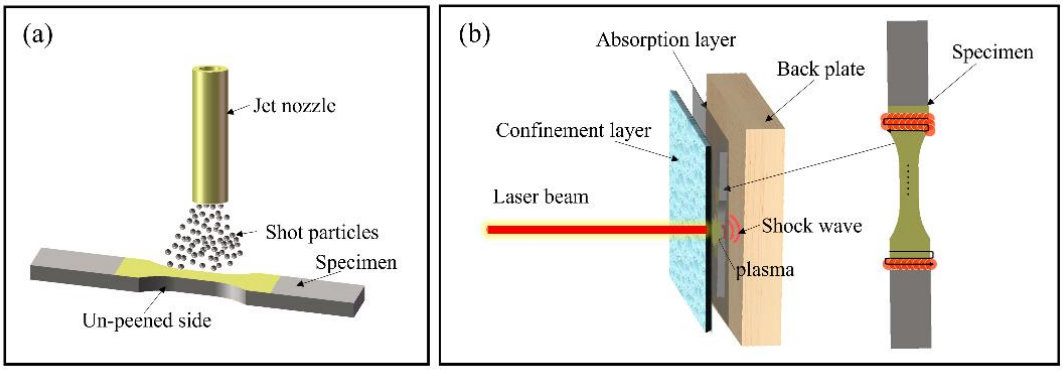

Fig. 2. Schematic of the (a) SP process and (b) LSP process.

2.2 Fatigue tests

To investigate the fatigue life enhancement by the combined surface treatment of SP+LSP, both fatigue tests and fatigue crack growth (FCG) tests were conducted, and the results were compared to the specimens with only SP treatment. For the fatigue test, the normal specimens (Fig. 3(a)), whose geometries are shown in Fig. 3(b), were tested under stress-control using a 50 kN MTS machine with a stress ratio of R = -1 and a frequency of 10 Hz at room temperature (Fig. 3(c)).

For the FCG test, the FCG tests are conducted by the K-decreasing method with a stress ratio of R=0.1 and a frequency of 10 Hz under loading control according to ASTM E647-15e1 [33] to investigate the difference in fatigue crack propagation behaviors near the threshold region between SP and SP+LSP specimens. The M(T) specimens (Fig. 3(d) and Fig. 3(e)) were tested using a 100 kN MTS machine at room temperature. Specimens were first fatigue pre-cracked for a minimum of 1 mm from the notch tip. Then the load shedding was performed to reduce load from the maximum load of 18kN toward the threshold region. This method have been widely used to characterize fatigue crack propagation near the threshold [34-36]. In the FCG test, the crack length was monitored by digital image correlation at 1 frame per second with a resolution of 2448×2408 pixels.

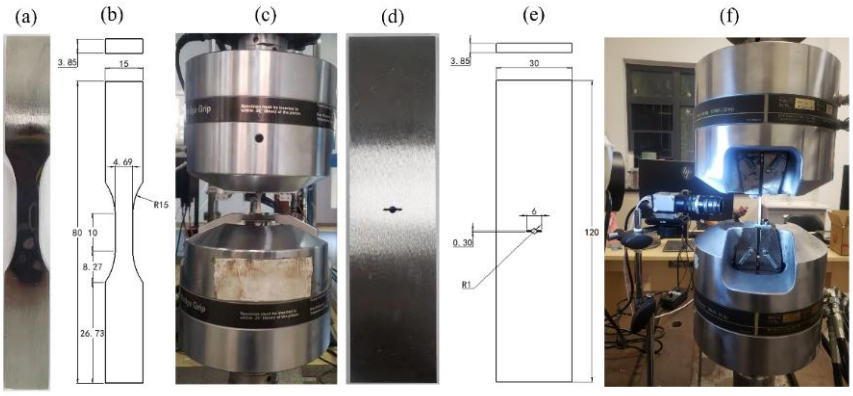

Fig. 3. (a) Normal specimen; (b) normal specimen geometries; (c) fatigue test setup; (d) M(T) specimen; (c) M(T) specimen geometries; (f) FCG test setup.

2.3 Surface and microstructure characterizations

To understand the mechanisms associated with fatigue performance enhancement, surface roughness, residual stress profile, microstructural evolution, and SP+LSP specimens were studied and compared with the baseline SP specimen. A Bruker 3D probe profilometer was employed to acquire the 3D surface topographies of these specimens by contact scanning over a sampling surface area of 0.5×0.5 mm^2 with an accuracy of 1 μm. In addition, a TR 2000 surface roughness tester was used to evaluate the arithmetic average height *R*a for the sampling surface area to quantify the surface roughness. For residual stress and full width at half maxima (FWHM), X-ray diffraction (XRD) measurement with Cr-Kα radiation (Rigaka AutoMATE II) was conducted on specimens after their surface layers were electrolytically removed. The XRD measurement was operated with a 40 kV voltage and 40 mA current using with a diameter of 1 mm and an exposure time of 30 s. And the direct refinement solution (DRS) method was applied on Fe (211) diffracting plane for stress evaluation with $\varphi_0 = 35°$ and the diffraction angle $2\theta = 156°$. To characterize the microstructure with the respective applied surface treatments, electron backscatter diffraction (EBSD) analysis was conducted using an Oxford Instruments (Symmetry

EBSD) with a step size of 0.03 μm to study the near-surface microstructure along the impact direction. The analysis depth was approximately 15 μm from the surface. Furthermore, transmission electron microscopy (TEM; FEI-Tecnai G2 F20 S-Twin) was employed to study the microstructural evolution.

3. Results and discussion

3.1 Fatigue test results

To investigate the effect of SP+LSP treatment on the properties of 30CrMnSiA steel, S-N curves at room temperature of SP+LSP specimens (Fig. 4(b)) were derived from the fatigue tests and compared to those of the SP specimen (Fig. 4(a)). The scatter bands were calculated by taking the confidence level equal to 95% and assuming a log-normal distribution of the number of cycles to failure for each stress level. Table 2 shows the scatter index that referred to a probability of survival in the range of 5–95% with the stress amplitude. The stress-based scatter index (T) of the endurance limit range for the possibility of survival (PS) = 95% and PS = 5% is a parameter used to evaluate the level of scattering associated with a population of fatigue data. It is noted that the value of T in the specimens with SP treatment alone was about 1.23, while the value of the specimens with the SP+LSP treatment was 1.11. The scatter band of the fatigue life of specimens with SP+LSP treatment was narrower than that of SP, as demonstrated in Figs. 4(a) and (b). This indicates that the SP+LSP treatment produced a lower fatigue life dispersibility than the SP treatment only.

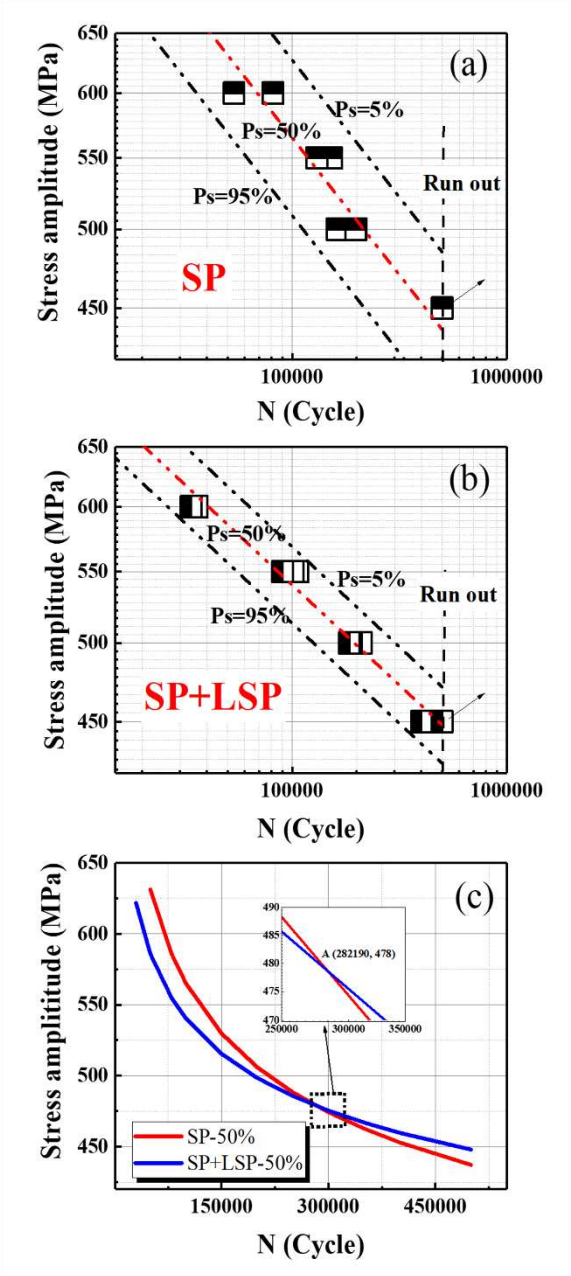

Fig. 4. Comparison of S-N curves for SP and SP+LSP specimens: (a) the scatter band of SP specimen; (b) the scatter band of SP+LSP specimen; (c) comparison of experimental failure lives of SP and SP+LSP specimens for 50% survival probability.

A comparison of the fatigue life of specimens with the SP and SP+LSP treatments for a 50% survival probability is presented in Fig. 4(c). A fatigue life transition behavior was observed when the maximum stress amplitude level was close to 478 MPa, which indicates that the combination of SP and LSP treatments did not always improve the fatigue performance. This means that the SP+LSP treatment only

improved the fatigue performance under low applied stress values or in the regime of high cycle fatigue (HCF). Under larger stress values or in the regime of low cycle fatigue (LCF), SP treatment gave better fatigue enhancement. This phenomenon was also observed in 2024-T351 aluminum alloy [26], but the mechanism responsible for this was not investigated.

Table 2. Detailed data of S-N curves of SP and SP+LSP specimens.

Specimen type	σ_A (MPa)			*T*	*K*
	$\sigma_{A,50\%}$	$\sigma_{A,95\%}$	$\sigma_{A,5\%}$		
SP specimen	391.44	352.77	434.36	1.23	6.27
SP+LSP specimen	413.24	392.65	434.91	1.11	8.58

To further investigate the different fatigue behaviors of the SP and SP+LSP specimens, the curves of the FCG rate versus a range of applied stress intensity factors were obtained under the small scale-yielding condition in the near-threshold region (Fig. 5) according to ASTM E647-15e1 [33]. The SP+LSP specimen shows a lower FCG rate than the SP specimen which indicates that the physically short cracks were retraded after LSP treatment according to the Santus model [37]. The elastic-plastic fracture mechanics characterized the propagation behavior, showing that both the microstructure and applied stress level are important for fatigue crack propagation [38]. Therefore, the modified microstructure plays an important role in retarding the initiation and growth of physically short cracks for the SP+LSP specimens compared with the SP specimens under the same loading conditions. This indicated that the higher fatigue fracture resistance for SP+LSP specimens in the short crack growth region which can explain this fatigue life transition behavior.

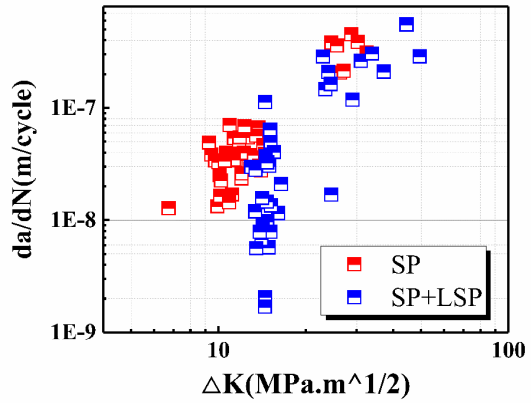

Fig. 5. Comparison of the fatigue crack growth rate (FCGR) curves in the near-threshold region for the SP and SP+LSP specimens.

3.2 Surface topographies and residual stress

The three-dimensional morphology of the surfaces of the SP and SP+LSP specimens was obtained by a 3D probe profilometer (Fig. 6). The roughness parameters measured from the experiments are listed in Table 3. It can be seen that the surface roughness of the SP+LSP specimens was smaller than that of SP specimens, as predicted. As shown in Figs. 6(b) and (c), the pit size decreased after LSP treatment. The variance, σ^2, decreased from 0.0331 to 0.0038 for the SP+LSP specimen, which means that a higher-quality surface morphology was obtained after LSP treatment. This shows that reversing the treatment order, i.e., SP followed by LSP, can significantly improve the surface roughness compared with the LSP+SP treatment [9]. According to previous work [10, 12, 21], pits on the surface aggravate surface stress concentration, which might accelerate the nucleating trend of fatigue cracks. Therefore, it is assumed that the fatigue crack initiation may be restricted with the improved the surface quality when applying LSP after SP.

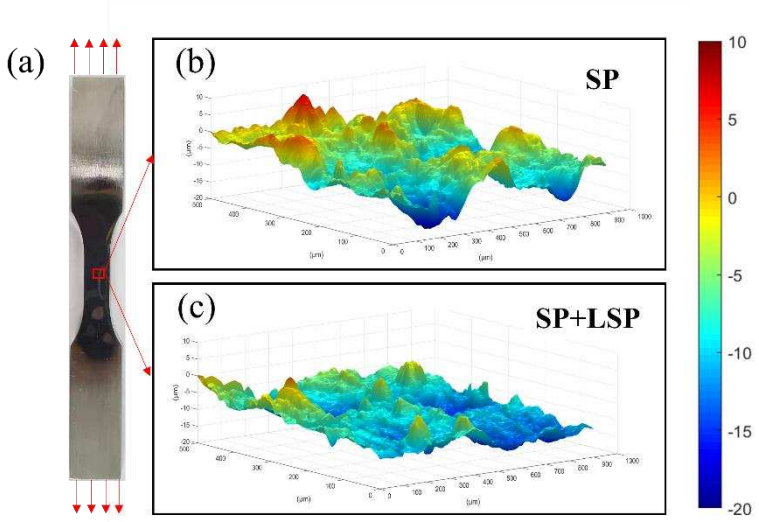

Fig. 6. (a) The S-N fatigue specimen; the characterization of the three-dimensional surface morphologies of (b) SP specimen and (c) SP+LSP specimen.

Table 3. Roughness characterization parameters.

Strengthening procedure	*Ra* (μm)	σ^2
SP	2.7067	0.0331
SP+LSP	2.6590	0.0038

The distribution of the induced CRS from the treated surface into the depth of the bulk material is shown in Fig. 7(a). The peak CRS was reached on the surface of both specimen types with a similar value. The distribution of CRS decreased gradually from the surface into the bulk material for both specimen types. In the Fig. 7(a), the CRS shift to the tensile residual stress in the depth of about 275 μm in SP specimen, but for the SP+LSP specimen, the residual stress is still in a compression state in the depth of 400 μm, which indicates that a deeper compressive residual stress layer is introduced after combination with the LSP treatment. In addition, the residual stress of un-peened specimen is shown in Fig. 7(a), a tensile residual stress gradually reduced to zero as the depth increases which can be attributed to the excessive polishing process before the surface treatments. Moreover, the CRS fluctuation can be

observed in the SP+LSP specimen which can be contributied to reflection and refraction of the shock wave when it propagates across an interface (boundaries or defects) [39]. In conclusion, the surface roughness and CRS values indicate a higher surface integrity for the SP+LSP specimens.

The FWHM results of both SP and SP+LSP specimens in Fig. 7(b) decrease monotonically with increasing depth into the bulk material. However, the FWHM values of the surface of the SP+LSP specimens were slightly smaller than those of the specimens with only SP treatment with the measurement error is about ±0.03°. In addition, the FWHM of un-peened specimen is shown in Fig. 7(b). It can be observed that the initial value of FWHM before peening treatment is about 1.3°~1.4°. The FWHM is mainly affected by crystallite size and dislocation density which can assess the plastic deformation zone to a certain extent [40-43]. It indicated that a increase grain size on the surface and a deeper plastic deformation layer after combination with LSP treatment. In addition, in order to more accurately measure the depth of plastic deformation after surface treatment, the inverse pole figures (IPF) are added (Fig. A.2). It can be observed that the depth of plastic deformation for SP and SP+LSP specimens are about 100 μm and 120 μm, respectively, indicating that the depth of plastic deformation zone has been significantly increased after combination with LSP treatment.

Under cyclic loading, the CRS induced by SP and LSP might be server relax when the applied load exceeds the maximum value of compressive residual stress [44-46], while the near-surface microstructure remains almost stable. This suggests that the near-surface microstructure plays a more significant role in determining the fatigue behavior than CRS [47]. Therefore, the microstructural evolution of the SP and SP+LSP specimens was compared in the following section.

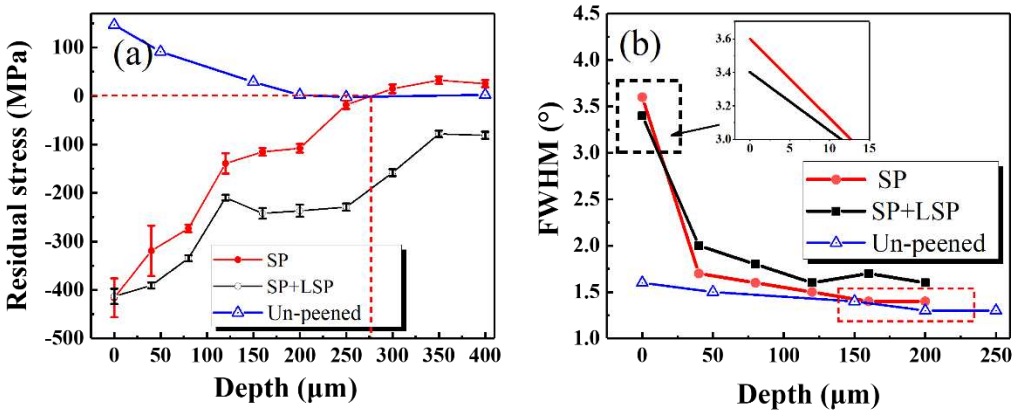

Fig. 7. The in-depth profile of (a) residual stress and (b) FWHM in SP and SP+LSP specimens.

3.3 Microstructures

The surface topographies and residual stress are only slightly improved after combination with LSP treatment. Therefore, the modified microstructures of SP and SP+LSP need to be systematically studied to explain the fatigue life transition behavior.

EBSD and TEM analyses were conducted on the SP and SP+LSP specimens to investigate the microstructural evolution before and after treatment. The grain size, shape, grain boundary, IPF maps, and Schmid factor were derived and adopted to investigate the effects of SP+LSP and SP treatments.

In the EBSD results, no Kikuchi diagrams [12, 14] were found on the impacted surface with no index points for either SP and SP+LSP specimens (Figs. 8 and 9) (white and black areas). The SP specimen had a larger area without the Kikuchi diagram, indicating more grain refinement on the surface compared with the SP+LSP specimen. This is also in accordance with the FWHM results in Fig. 7(b). In addition, a large gradient structure was observed in both SP and SP+LSP specimens.

According to the grain morphology, two regions were specified in Fig. 8(a): I-surface and II-subsurface. For the SP specimens, ultra-fine grains were found in the I-surface region, and elongated and flattened grains were observed in the II-subsurface region. Similar situations were observed in aluminum

alloys AA7075-T7351 and AA2024-T351 [12, 48]. In contrast, ultra-fine grains were found in the II-subsurface region in the SP+LSP specimen (Fig. 8(d)), showing a heterogeneous microstructure.

To quantify the difference in grain morphologies between the SP and SP+LSP specimens, the Gaussian distributions of grain morphology were derived and shown in Figs. 8(c) and (f) for the I-surface region of the SP specimen, II-subsurface region of SP specimen, I-surface region of the SP+LSP specimen, and II-subsurface region of the SP+LSP specimen, respectively. The major difference was in the II-surface region, where the average grain rectangularity of the II-subsurface zone was 0.5908 in the SP specimen, whereas it was 0.6680 in the SP+LSP specimen.

The maps of the grain boundaries are shown in Figs. 8(b) and (e) for SP and SP+LSP specimens, respectively. There were many HAGBs on the I-surface region of the SP specimen, which was not true for the SP+LSP specimen because the high strain rate caused grain torsion and formed HAGBs [11, 49]. The percentage of grain boundaries of >2°, >5°, and >15° are listed in Table 4. After SP +LSP processing, the percentage of HAGBs increased from 74.2% to 80.6% in the I-surface zone, and there was also a slight increase in the subgrain boundaries in the II-subsurface.

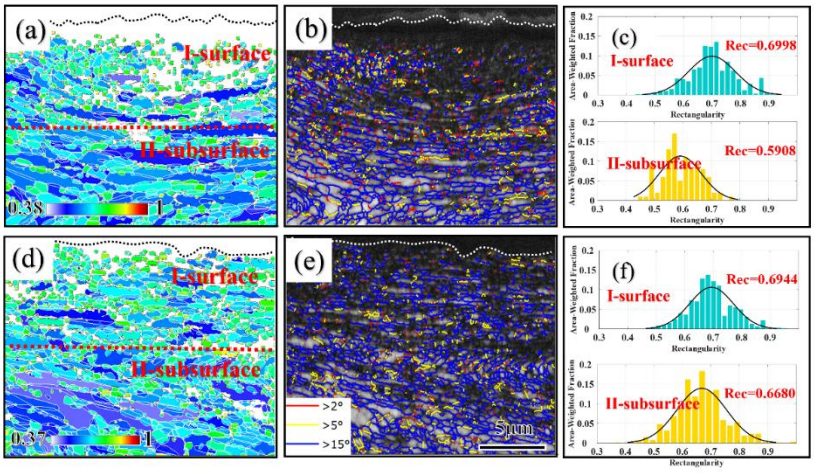

Fig. 8. Cross-sectional EBSD images of (a) the grain shape for the SP specimen; (b) grain boundaries for the SP specimen; (c) the Gaussian distribution of grain shape for the SP specimen and (d) the grain

shape for the SP+LSP specimen; (e) grain boundaries for the SP+LSP specimen; (f) the Gaussian distribution of grain shape for the SP+LSP specimen.

Table 4. The percentage of grain boundary orientations.

Grain boundary	SP specimen		SP+LSP specimen	
	I-surface	II-subsurface	I-surface	II-subsurface
>2°	15.4%	11.0%	12.1%	10.9%
>5°	10.4%	6.54%	7.21%	7.04%
>15°	74.2%	82.5%	80.6%	82.0%

Furthermore, the lattice orientation and Schmid factor played a significant role in determining crystal-scale stress distributions under cyclic loads in which fatigue cracks usually nucleate in the well-oriented grains near surfaces with a high Schmid factor, especially in the HCF [6]. The IPF and Schmid factor maps for SP and SP+LSP specimens are shown in Fig. 9. Fig. 9(a) shows the micro-texture alteration in the thickness direction of the SP specimens with a <001> dominant texture at the surface which then evolved into <111>, and, finally, to <101> in the subsurface. However, the micro-texture of the SP+LSP specimen did not show this change and instead showed randomly-orientated grains which was attributed to the laser-induced shock wave. This random orientation of grains is associated with a higher hysteresis effect and complex stress state [50]. Furthermore, in the SP+LSP specimen, a decreasing Schmid factor was observed from the surface to the subsurface; however, the Schmid factor of the SP specimen remained relatively constant. The Gaussian distributions of the Schmid factor of the SP and SP+LSP specimens are shown in Figs. 9 (b) and (d), with respective peak values of 0.4777 and 0.4516.

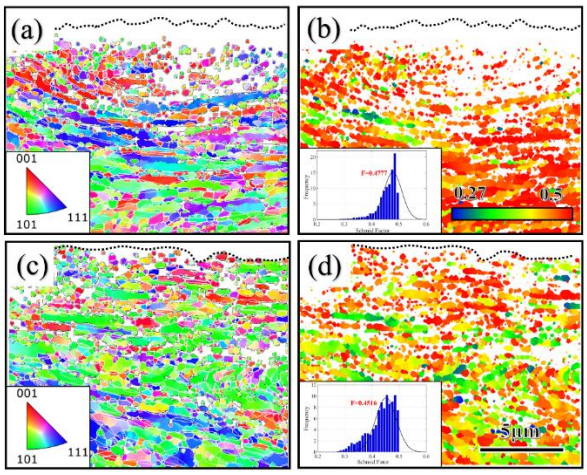

Fig. 9. (a) IPF of the SP specimen, (b) Schmid factor maps and Gaussian distribution of Schmid factor of the SP specimen, (c) IPF of the SP+LSP specimen, and (d) Schmid factor maps and Gaussian distribution of Schmid factor of the SP+LSP specimen.

TEM was employed to investigate the grain and dislocation structures in detail to study the microstructural evolution after LSP treatment. The TEM maps of the subsurface and regions were obtained for SP (Figs. 10(a) and (b)) and SP+LSP (Figs. 10(c) and (d)) specimens. For the SP+LSP specimen (Fig. 10(c)), ultra-fine grains were observed with clear recrystallization characteristics, in contrast to the elongated and flattened grains in the SP specimen (Fig. 10(a)). These findings are consistent with the EBSD results in Figs. 8(a) and (d). In addition, as shown in Figs. 10(b) and (d), statistically stored dislocations introduced by SP treatment were found in a deeper location after LSP. They transformed into high-density dislocations, dislocation tangles, and sub-boundaries, resulting in finer grains.

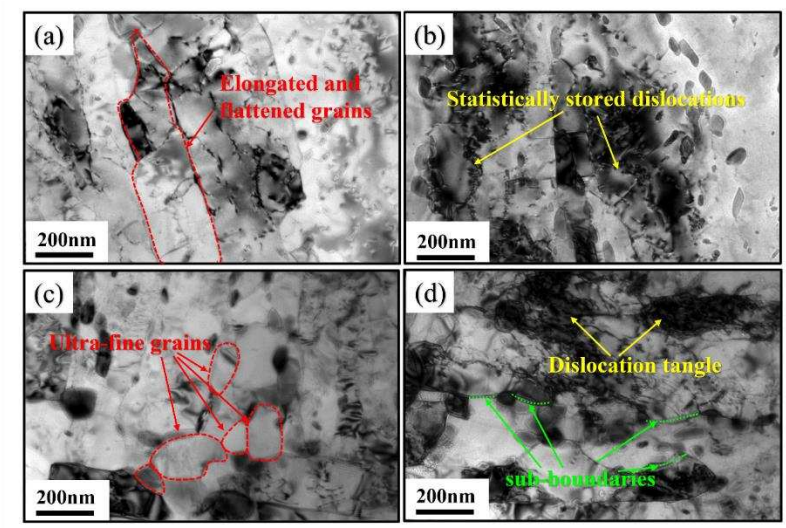

Fig. 10. Bright-field TEM micrographs of (a) the subsurface of the SP specimen , (b) the region below, (c) the subsurface of the SP+LSP specimen , and (d) the region below.

3.4 Fatigue fracture surface

The fracture surfaces after fatigue tests with a stress amplitude of 500 MPa were studied via scanning electron microscope (SEM) to investigate differences in the fatigue behavior between the SP and SP+LSP specimens. As shown in Fig. 11(a) and Fig. 12(a), the fracture surfaces can be divided into three regions for both specimens, i.e., fatigue crack initiation (FCI) region, fatigue crack propagation region, and final fracture region. However, in the fatigue crack propagation region of the SP+LSP specimen, two different crack propagation behaviors were observed in Fig. 12(a). This indicates a transition of the fatigue crack propagation rate compared to the SP specimen due to the heterogeneous microstructure produced by the SP+LSP processing (also see Section 3.3 ESBD results).

The crack initiation sites were located on the free surface for both specimens, as shown in Fig. 11(b) and Fig. 12(b). However, there were no obvious nucleation sites in the SP specimen (Fig. 11(b)) due to the intergranular fracture being the dominant failure mode with the nanograins at the surface. In the SP+LSP specimen, obvious crack nucleation sites as well as significant transgranular propagation

characterization with roughness morphology can be observed due to the random grain orientation near the surface.

For SP specimen, when a crack extended to the (c) zones (Fig. 11(c)), fatigue steps were observed in the SP specimen, indicating brittle fatigue fracture by the nanograins on the surface introduced by the SP treatment. However, contrary to the findings in the SP specimen, only fatigue striation was found in the SP+LSP specimen (Fig. 12(c)), showing ductile fracture and indicating slower fatigue crack propagation.

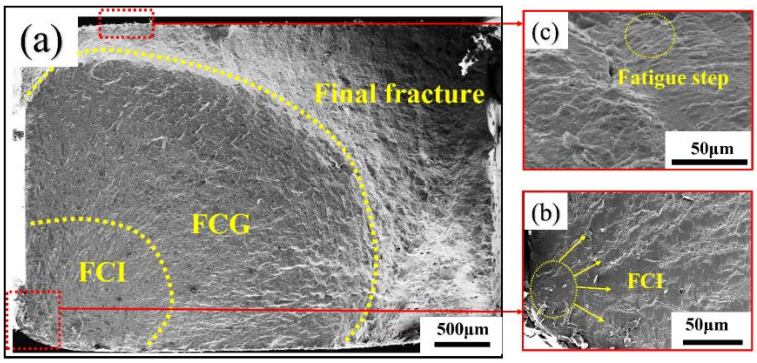

Fig. 11. The fracture surface of the SP specimen: (a) complete morphology of the fracture surface; (b) details of fatigue crack initiation; (c) details of the SP-treated surface region.

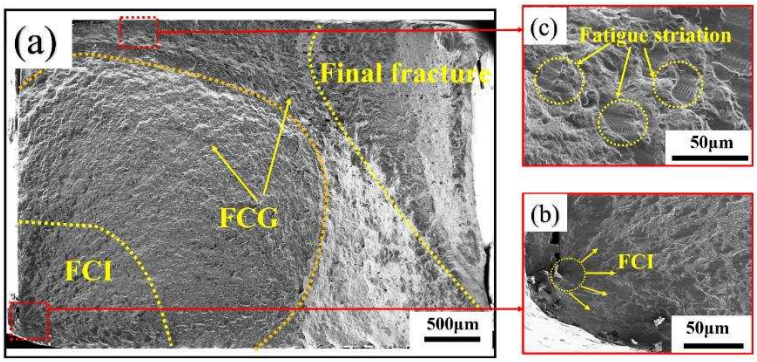

Fig. 12. The fracture surface of the SP+LSP specimen: (a) complete morphology of the fracture surface; (b) details of fatigue crack initiation; (c) details of the SP+LSP-treated surface region.

3.5 Microstructural fatigue mechanisms

The fatigue tests of the specimen with SP and SP+LSP treatments demonstrate a transition point to a stress level, above which SP treatment resulted in a better fatigue life than the SP+LSP treatment and below which the SP+LSP treatment was better. To understand this transition, the microstructural evolution was investigated in detail in Section 3.4. These microstructural evolutions operated differently in the fatigue process, namely, crack incubation, microstructurally short crack growth, physically short crack growth, and long crack growth.

For crack incubation, the experimental results indicated that a finer-grained material generally has a longer fatigue life, since persistent slip bands are difficult to form [51-53]. Furthermore, the crack incubation life can be modeled by the Tanaka and Mura theory [54]:

$$N_{\text{incubation}} = \frac{\alpha}{d \times \Delta\varepsilon_{\text{p}}^2}, \tag{1}$$

where α is a constant, d is the grain size, and $\Delta\varepsilon_{\text{p}}$ is the macroscopic plastic strain range. A smaller grain size results in a longer crack initiation time; therefore, the SP specimen with a finer grain size on the surface had a longer fatigue incubation life and should have a longer fatigue life than the SP+LSP specimen. In the S-N curve (Fig. 4), however, under a stress level of 478 MPa (HCF), the total fatigue life of the SP specimen was shorter than the SP+LSP specimen because of additional short crack behavior in the latter.

Under a low-stress level, the cyclic plastic strain was localized in regions with a heterogeneous microstructure in which cyclic microplastic deformation accumulated, but regions outside these localized plastic zones were mainly elastic [2, 7]. In this manner, the microstructurally short cracks played an important role in determining the fatigue life of the HCF [7, 55].

In addition, short cracks propagated by plastic slip, which is sensitive to the efficient resolved shear stress [6, 56]. The efficient resolved shear stress is the driving force for the plastic slip on the slip system τ_{eff} and can be calculated by:

$$\tau_{\mathrm{eff}} = \tau - \tau_{\mathrm{b}}, \tag{2}$$

where τ is the resloved shear stress as the total driving force for dislocation slip; τ_{b} is the kinematic back-stress which acts to suppress dislocation slip and is caused by dislocation pile-up in the heterogeneous microstructure and at grain boundaries for gradient structures. The resolved shear stress τ is proportional to the Schmid factor following Schmid's law. Therefore, the lower Schmid factor in the SP+LSP specimen (Fig. 9(d)) effectively reduced the total driving force for dislocation slip.

For the 30CrMnSiA steel with a polycrystalline structure, the plastic slip rate $\dot{\gamma}$ can be described according to the J_2-flow theory [57, 58]:

$$\dot{\gamma} = \left(\frac{3}{2}\right)^{\frac{m+1}{2}} \dot{\gamma}_0 \left(\frac{\left|\tau - \tau_{\mathrm{b}}\right|}{\sigma_{\mathrm{r}}} \right)^{m} \mathrm{sgn}(\tau - \tau_{\mathrm{b}}), \tag{3}$$

where m is a material constant, $\dot{\gamma}_0$ is the reference shear rate, and σ_{r} is the slip resistance given as [13]:

$$\sigma_{\mathrm{r}} = \sigma_{\mathrm{Y}} + M\eta\mu b\sqrt{\rho} + \tau_{\mathrm{b}} + \frac{k_{\mathrm{th}}}{\sqrt{d}}, \tag{4}$$

where M is the Taylor factor, η is a material constant, N is the total number of pile-up dislocations, μ is the shear modulus of the matrix, b is the Burger vector, d is the grain size, and k_{th} is the Hall-Petch slope. It is seen that the kinematic back-stress can affect σ_{r} and $\dot{\gamma}$. Eq. (3) shows that increasing the back-stress can significantly reduce the plastic slip rate.

For the investigated 30CrMnSiA, the sources of kinematic back-stress τ_{b} are (i) dislocation tangles, (ii) grain boundaries, and (iii) cementite particles [5]; therefore, the kinematic back-stress of 30CrMnSiA steel can be expressed as:

$$\tau_{\mathrm{b}}=\underbrace{\frac{M\mu}{1-\nu}\sqrt{\frac{0.45\theta b}{2\pi d_{\mathrm{t}}}}}_{\text{dislocation tangle and cell}}+\underbrace{\frac{Mb\mu}{\alpha d}N_{\mathrm{d}}}_{\text{grain boundaries}}+\underbrace{\tau_{\mathrm{p}}}_{\text{cementite particles}}, \tag{5}$$

where θ is the misorientation angle between HAGBs, d_{t} is the distance of dislocation tangles and cells, ν is Poisson's ratio, N_{d} is the number of dislocations in the pile-up, and τ_{p} is the kinematic back-stress caused by cementite particles.

For microstructurally short crack propagation, microstructural fracture mechanics are used to characterize the fatigue crack propagation behavior of fracture modes II and III. The FCGR can be described as [38]:

$$\frac{\mathrm{d}a}{\mathrm{d}N}=\varphi\Delta\gamma^{p}(D-a), \tag{6}$$

where φ and p are material constants; D is the distance of strong microstructural barriers, such as grain boundaries, dislocation tangles, and cementite particles; a is the crack length. Under a single cycle, changes in the crack length a can be neglected, so the kinematic back-stress τ_{b} and slip resistance σ_{r} remain the same. If considering one-dimensional fatigue propagation, the plastic slip range can be described for a loading cycle, and the time interval is $\Delta t=1/f$, where f is the loading frequency, and the accumulative shear strain is:

$$\Delta\gamma=\int_{0}^{\Delta t}\dot{\gamma}dt. \tag{7}$$

By combining Eq. (3), the accumulative shear strain in Eq. (7) simplifies to:

$$\Delta\gamma=\left(\frac{3}{2}\right)^{\frac{\mathrm{m}+1}{2}}\dot{\gamma}_{0}\frac{1}{\sigma_{\mathrm{r}}^{\mathrm{m}}}\int_{0}^{\Delta t}\left[\left|\tau-\tau_{\mathrm{b}}\right|^{\mathrm{m}-1}(\tau-\tau_{\mathrm{b}})\right]dt. \tag{8}$$

The FCGR for microstructurally short crack can be obtained by combining Eqs. (6) and (8):

$$\frac{\mathrm{d}a}{\mathrm{d}N}=(D-a)\varphi\left(\frac{3}{2}\right)^{\frac{\mathrm{m}+1}{2}}\dot{\gamma}_{0}\frac{1}{\sigma_{\mathrm{r}}^{\mathrm{m}}}\int_{0}^{\Delta t}\left[\left|\tau-\tau_{\mathrm{b}}\right|^{\mathrm{m}-1}(\tau-\tau_{\mathrm{b}})\right]dt, \tag{9}$$

As shown in Eq. (9), the microstructurally short crack can be retarded by increasing the kinematic back-

stress τ_b and slip resistance σ_r and decreasing the distance of the strong microstructural barrier *D*.

In this study, to reexamine Figs. 8(e) and 10(d) for the SP+LSP specimen, more HAGBs and dislocation tangles were observed than in Figs. 8(b) and Fig. 10(b) for the SP specimen. These significantly improved the kinematic back-stress and a lower FCGR can be obtained. Another factor that decreased FCG rate in the SP+LSP specimen was the ultra-fine grains (Figs. 8(d) and 10(c)). Furthermore, the lower Schmid factor in the SP+LSP specimen (Fig. 9(d)) can effectively reduce the total driving force and then reduced the FCGR. Therefore, it can be concluded that by considering Eq. (9), the microstructural short cracks were effectively retarded in the SP+LSP specimen by decreasing the driving force and increasing the slip resistance.

The above discussion explains the transition behavior for the fatigue performance of SP and SP+LSP specimens. The microstructure of the SP and SP+LSP specimens were different under high and low stress levels, which can be explained by the nature of the distribution of crack incubation and microstructurally small crack growth. Under a high stress level, plasticity was induced in each cycle [1, 4], and bulk plastic deformation occurred, which involved several grains. Then, the crack growth rate for cracks at each incubation site was proportional to the length of each crack [4]. This process indicates the fatigue life of crack incubation is dominant at high-stress level. However, under a low-stress level, both crack incubation and microstructurally short crack propagation life dominate the fatigue life. The EBSD and TEM results showed that the increased number of HAGBs, lower Schmid factor, higher dislocation density, and ultra-fine grains in the SP+LSP specimen effectively retarded the microstructurally short crack propagation. The SP+LSP specimen displayed a lower FCG rate in Fig. 5 than the SP specimen, which also indicated that physically short cracks were retraded after combination with LSP treatmet. This can be contributed to the large number of defects (high-density dislocations, dislocation tangles, and sub-

boundaries) occured after LSP which may act as a strong barrier to pile-up the dislocations emitted from the crack tips [59, 60].

4. Conclusions

In this work, the fatigue life enhancement after SP+LSP treatment was studied and compared with a baseline SP treatment for a typical medium carbon steel (quenched and tempered 30CrMnSiA steel). The fatigue properties were investigated experimentally and analyzed by a series of parameters such as surface morphology, surface roughness, residual stress, and microstructural evolution. The different fatigue failure mechanisms were identified and studied. The main conclusions are as follows.

1. A fatigue life transition stress level of 478 MPa was observed, which indicates different fatigue mechanisms and the enhancement of SP specimens and SP+LSP specimens in HCF and LCF.
2. A significant gradient structure was observed in both SP and SP+LSP specimens. Nano-grains were observed on the surface of the SP specimen, but ultra-fine grains were introduced at a deeper level in the SP+LSP specimen and formed a heterogeneous structure. In addition, after LSP, the number of HAGBs increased, and the Schmid factor decreased. The TEM results indicated that after LSP treatment, the statistically-stored dislocations introduced by SP treatment transformed to other state with high-density dislocations, dislocation tangles, and sub-boundaries.
3. The SP specimen had a longer fatigue incubation life than the SP+LSP specimen due to nanograins on the surface. However, the microstructurally short crack propagation life became significant after LSP treatment due to the modified microstructure in the SP+LSP specimen. These microstructural evolutions functioned differently during fatigue crack incubation, and microstructurally short crack propagation can explain the fatigue life transition behavior.

5. Acknowledgment

The financial support of the National Natural Science Foundation of China (Grant No. 51401028, No.51271193, No. 11402277, No. 11790292), the Strategic Priority Research Program of the Chinese Academy of Sciences (Grant No. XDB22040303), and the Innovation Program (237099000000170004).

Appendix A

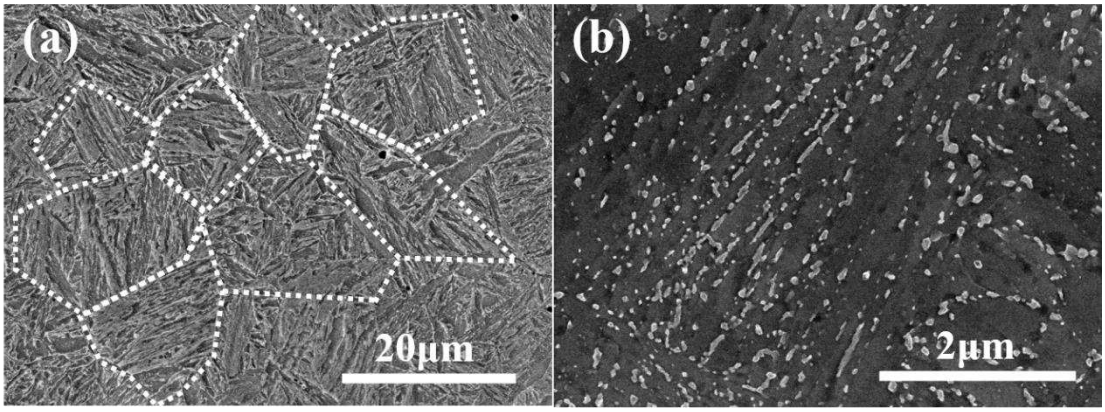

Fig. A.1. SEM images of the microstructures of the 30CrMnSiA steel.

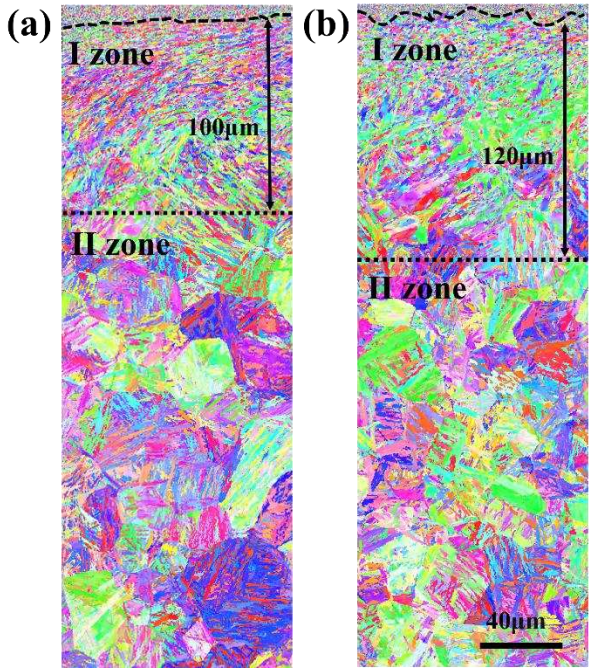

Fig. A.2. Cross-sectional EBSD images of IPF for SP (a) and SP+LSP (b) specimens.

References

[1] M.D. Sangid. The physics of fatigue crack initiation. Int J Fatigue 2013; 57: 58-72. https://doi.org/10.1016/j.ijfatigue.2012.10.009.

[2] C.A. Sweeney, W. Vorster, S.B. Leen, E. Sakurada, P.E. McHugh, F.P.E. Dunne. The role of elastic anisotropy, length scale and crystallographic slip in fatigue crack nucleation. J Mech Phys Solids 2013; 61: 1224-1240. https://doi.org/10.1016/j.jmps.2013.01.001.

[3] H. Li, G. Kang, C. Yu. Modeling uniaxial ratchetting of magnesium alloys by a new crystal plasticity considering dislocation slipping, twinning and detwinning mechanisms. Int J Mech Sci 2020; 105660. https://doi.org/10.1016/j.ijmecsci.2020.105660.

[4] D. McDowell, K. Gall, M. Horstemeyer, J. Fan. Microstructure-based fatigue modeling of cast A356-T6 alloy. Eng Fract Mech 2003; 70: 49-80. https://doi.org/10.1016/S0013-7944(02)00021-8.

[5] R.A. Barrett, P.E. O'Donoghue, S.B. Leen. A physically-based constitutive model for high temperature microstructural degradation under cyclic deformation. Int J Fatigue 2017; 100: 388-406. https://doi.org/10.1016/j.ijfatigue.2017.03.018.

[6] M. Sauzay, T. Jourdan. Polycrystalline microstructure, cubic elasticity, and nucleation of high-cycle fatigue cracks. Int J Fract 2006; 141: 431-446. https://doi.org/10.1007/s10704-006-9005-x.

[7] M. Shenoy, J. Zhang, D.L. McDowell. Estimating fatigue sensitivity to polycrystalline Ni-base superalloy microstructures using a computational approach. Fatigue Fract Eng M 2007; 30: 889-904. https://doi.org/10.1111/j.1460-2695.2007.01159.x.

[8] M. Shenoy, Y. Tjiptowidjojo, D. McDowell. Microstructure-sensitive modeling of polycrystalline IN 100. Int J Plast 2008; 24: 1694-1730.
https://doi.org/10.1016/j.ijplas.2008.01.001.

[9] X. Luo, N. Dang, X. Wang. The effect of laser shock peening, shot peening and their combination on the microstructure and fatigue properties of Ti-6Al-4V titanium alloy. Int J Fatigue 2021; 153.
https://doi.org/10.1016/j.ijfatigue.2021.106465.

[10] M. Benedetti, V. Fontanari, M. Bandini, E. Savio. High- and very high-cycle plain fatigue resistance of shot peened high-strength aluminum alloys: The role of surface morphology. Int J Fatigue 2015; 70: 451-462.
https://doi.org/10.1016/j.ijfatigue.2014.07.002.

[11] L. Chen, X. Ren, W. Zhou, Z. Tong, S. Adu-Gyamfi, Y. Ye, Y. Ren. Evolution of microstructure and grain refinement mechanism of pure nickel induced by laser shock peening. Mater Sci Eng: A 2018; 728: 20-29.
https://doi.org/10.1016/j.msea.2018.04.105.

[12] A. Gariépy, F. Bridier, M. Hoseini, P. Bocher, C. Perron, M. Lévesque. Experimental and numerical investigation of material heterogeneity in shot peened aluminium alloy AA2024-T351. Surf Coat Tech 2013; 219: 15-30.
https://doi.org/10.1016/j.surfcoat.2012.12.046.

[13] J. Zhao, X. Lu, F. Yuan, Q. Kan, S. Qu, G. Kang, X. Zhang. Multiple mechanism based constitutive modeling of gradient nanograined material. Int J Plast 2020; 125: 314-330.
https://doi.org/10.1016/j.ijplas.2019.09.018.

[14] D.J. Child, G.D. West, R.C. Thomson. Assessment of surface hardening effects from shot peening

on a Ni-based alloy using electron backscatter diffraction techniques. Acta Mater 2011; 59: 4825-4834. https://doi.org/10.1016/j.actamat.2011.04.025.

[15] N. Kashaev, V. Ventzke, M. Horstmann, S. Chupakhin, S. Riekehr, R. Falck, E. Maawad, P. Staron, N. Schell, N. Huber. Effects of laser shock peening on the microstructure and fatigue crack propagation behaviour of thin AA2024 specimens. Int J Fatigue 2017; 98: 223-233. https://doi.org/10.1016/j.ijfatigue.2017.01.042.

[16] X.-k. Meng, H. Wang, W.-s. Tan, J. Cai, J.-z. Zhou, L. Liu. Gradient microstructure and vibration fatigue properties of 2024-T351 aluminum alloy treated by laser shock peening, Surface and Coatings Technology 2020; 391. https://doi.org/10.1016/j.surfcoat.2020.125698.

[17] I. Altenberger. Deep rolling–the past, the present and the future. Conf Proc: ICSP 2005; 9: 144-155.

[18] T. Chakherlou, J. Vogwell. The effect of cold expansion on improving the fatigue life of fastener holes. Engineering failure analysis 2003; 10: 13-24. https://doi.org/10.1016/S1350-6307(02)00028-6.

[19] K. Lu, J. Lu. Nanostructured surface layer on metallic materials induced by surface mechanical attrition treatment. Mate Sci Eng: A 2004; 375-377: 38-45. https://doi.org/10.1016/j.msea.2003.10.261.

[20] N. Kumar, G.P. Chaudhari, S.R. Meka. Influence of Ultrasonic Shot Peening on Microstructure, Mechanical, and Electrochemical Behavior of 316 Stainless Steel. J Mater Eng Perform 2021. https://doi.org/10.1007/s11665-021-06322-x.

[21] Y. Gao, W. Yang, Z. Huang, Z. Lu. Effects of residual stress and surface roughness on the fatigue life of nickel aluminium bronze alloy under laser shock peening. Eng Fract Mech 2021; 244.

https://doi.org/10.1016/j.engfracmech.2021.107524.

[22] Y. Gao. Improvement of fatigue property in 7050–T7451 aluminum alloy by laser peening and shot peening. Mater Sci Eng: A 2011; 528: 3823-3828.

https://doi.org/10.1016/j.msea.2011.01.077.

[23] S.J. Lainé, K.M. Knowles, P.J. Doorbar, R.D. Cutts, D. Rugg. Microstructural characterisation of metallic shot peened and laser shock peened Ti–6Al–4V. Acta Mater 2017; 123: 350-361.

https://doi.org/10.1016/j.actamat.2016.10.044.

[24] G. Lu, L. Wang, H. Li, Z. Ji, Q. Wang, X. Pei, K. Sugioka. Methods for the suppression of “residual stress holes” in laser shock treatment. Mater Today Commun 2021; 28.

https://doi.org/10.1016/j.mtcomm.2021.102486.

[25] Y. Hu, C. Gong, Z. Yao, J. Hu. Investigation on the non-homogeneity of residual stress field induced by laser shock peening. Surf Coat Tech 2009; 203: 3503-3508.

https://doi.org/10.1016/j.surfcoat.2009.04.029.

[26] C. Rodopoulos, J. Romero, S. Curtis, E. de Los Rios, P. Peyre. Effect of controlled shot peening and laser shock peening on the fatigue performance of 2024-T351 aluminum alloy. J Mater Eng Perform 2003; 12: 414-419.

[27] P. Peyre, R. Fabbro, P. Merrien, H. Lieurade. Laser shock processing of aluminium alloys. Application to high cycle fatigue behaviour. Mater Sci Eng: A 1996; 210: 102-113.

https://doi.org/10.1016/0921-5093(95)10084-9.

[28] H. Soyama, C.R. Chighizola, M.R. Hill. Effect of compressive residual stress introduced by cavitation peening and shot peening on the improvement of fatigue strength of stainless steel. J Mater Process Tech 2021; 288.

https://doi.org/10.1016/j.jmatprotec.2020.116877

[29] H. Soyama, C.R. Chighizola, M.R. Hill. Effect of compressive residual stress introduced by cavitation peening and shot peening on the improvement of fatigue strength of stainless steel. J Mater Process Tech 2021; 288.

https://doi.org/10.1016/j.jmatprotec.2020.116877

[30] G. Ivetic, I. Meneghin, E. Troiani, G. Molinari, J. Ocaña, M. Morales, J. Porro, A. Lanciotti, V. Ristori, C. Polese, J. Plaisier, A. Lausi. Fatigue in laser shock peened open-hole thin aluminium specimens. Mat Sci Eng A-Struct 2012; 534: 573-579.

https://doi.org/10.1016/j.msea.2011.12.010

[31] S.H. Lim, Z. Zhang, D.H.L. Seng, M. Lin, S.L. Teo, F. Wei, A.K.H. Cheong, S. Wang, J. Pan. In-situ warm shot peening on Ti-6Al-4V alloy: Effects of temperature on fatigue life, residual stress, microstructure and mechanical properties. J Alloy Compd 2021; 882.

https://doi.org/10.1016/j.jallcom.2021.160701

[32] L. Xie, Y. Wen, K. Zhan, L. Wang, C. Jiang, V. Ji. Characterization on surface mechanical properties of Ti–6Al–4V after shot peening. J Alloy Compd 2016; 666: 65-70.

https://doi.org/10.1016/j.jallcom.2016.01.119

[33] ASTM E647-15e1, Standard test method for measurement of fatigue crack growth rates. ASTM International 2015.

[34] R. Bu, R. Stephens. Comparison of short and long fatigue crack growth in 7075 - T6 aluminum. Fatigue Fract Eng Mater Struct 1986; 9(1): 35-48.

https://doi.org/10.1111/j.1460-2695.1986.tb01209.x

[35] S. Kikuchi, T. Mori, H. Kubozono, Y. Nakai, M.O. Kawabata, K. Ameyama. Evaluation of near-

threshold fatigue crack propagation in harmonic-structured CP titanium with a bimodal grain size distribution. Eng Fract Mech 2017; 181: 77-86.

https://doi.org/10.1016/j.engfracmech.2017.06.026

[36] D. Peixoto, P. de Castro. Near threshold fatigue crack propagation in railways' steels: Comparison of two testing techniques. Theor Appl Fract Mec 2015; 80: 73-78.

https://doi.org/10.1016/j.tafmec.2015.06.008

[37] C. Santus, D. Taylor. Physically short crack propagation in metals during high cycle fatigue. Int J Fatigue 2009; 31: 1356-1365.

https://doi.org/10.1016/j.ijfatigue.2009.03.002

[38] K. Miller. The two thresholds of fatigue behaviour. Fatigue Fract Eng M 1993; 16: 931-939.

https://doi.org/10.1111/j.1460-2695.1993.tb00129.x.

[39] L. Zhou, Y. Li, W. He, G. He, X. Nie, D. Chen, Z. An. Deforming TC6 titanium alloys at ultrahigh strain rates during multiple laser shock peening. Mat Sci Eng A-Struct 2013; 578: 181-186.
https://doi.org/10.1016/j.msea.2013.04.070

[40] D. Dorset. X-ray diffraction: a practical approach. Microsc microanal 1998; 4: 513-515.

https://doi.org/10.1017/S143192769800049X.

[41] E. Maleki, O. Unal. Roles of surface coverage increase and re-peening on properties of AISI 1045 carbon steel in conventional and severe shot peening processes. Surf Interfaces 2018; 11: 82-90.

https://doi.org/10.1016/j.surfin.2018.03.003.

[42] E. Maleki, O. Unal, M. Guagliano, S. Bagherifard. The effects of shot peening, laser shock peening and ultrasonic nanocrystal surface modification on the fatigue strength of Inconel 718. Mater Sci Eng: A 2021. 810: 141029.

https://doi.org/10.1016/j.msea.2021.141029.

[43] R. Sun, Z. Che, Z. Cao, S. Zou, J. Wu, W. Guo, Y. Zhu. Fatigue behavior of Ti-17 titanium alloy subjected to different laser shock peened regions and its microstructural response. Surf Coat Tech 2021; 383.
https://doi.org/10.1016/j.surfcoat.2019.125284.

[44] J.-C. Kim, S.-K. Cheong, H. Noguchi. Evolution of residual stress redistribution associated with localized surface microcracking in shot-peened medium-carbon steel during fatigue test. Int J Fatigue 2013; 55: 147-157.
https://doi.org/10.1016/j.ijfatigue.2013.06.010.

[45] S. Yang, W. Zeng, J. Yang. Characterization of shot peening properties and modelling on the fatigue performance of 304 austenitic stainless steel. Int J Fatigue 2020; 137.
https://doi.org/10.1016/j.ijfatigue.2020.105621.

[46] M.A.S. Torres, H.J.C. Voorwald. An evaluation of shot peening, residual stress and stress relaxation on the fatigue life of AISI 4340 steel. Int J Fatigue 2002; 24: 877-886.
https://doi.org/10.1016/S0142-1123(01)00205-5

[47] L. Spadaro, S. Hereñú, R. Strubbia, G. Gómez Rosas, R. Bolmaro, C. Rubio González. Effects of laser shock processing and shot peening on 253 MA austenitic stainless steel and their consequences on fatigue properties. Opt Laser Technol 2020; 122: 105892.
https://doi.org/10.1016/j.optlastec.2019.105892.

[48] T. Honda, M. Ramulu, A. Kobayashi. Effect of shot peening on fatigue crack growth in 7075-T7351. ASTM International 2005.

[49] J.E. Field, S.M. Walley, W.G. Proud, H.T. Goldrein, C.R. Siviour. Review of experimental techniques for high rate deformation and shock studies. Int J Impact Eng 2004; 30: 725-775.

https://doi.org/10.1016/j.ijimpeng.2004.03.005.

[50] A. Manonukul, F. Dunne. High–and low–cycle fatigue crack initiation using polycrystal plasticity. Proceedings of the Royal Society of London. Series A: Mathematical. Physical and Engineering Sciences 2004; 460: 1881-1903.

https://doi.org/10.1098/rspa.2003.1258.

[51] A. Weidner, R. Beyer, C. Blochwitz, C. Holste, A. Schwab, W. Tirschler. Slip activity of persistent slip bands in polycrystalline nickel. Mater Sci Eng: A 2006; 435-436: 540-546.

https://doi.org/10.1016/j.msea.2006.07.039.

[52] H. Liu. A dislocation barrier model for fatigue limit–as determined by crack non-initiation and crack non-propagation. Int J Fract 1993; 96: 331-345.

[53] R. Keller, W. Zielinski, W.W. Gerberich. On the onset of low-energy dislocation substructures in fatigue: grain size effects. Mater Sci Eng: A 1989; 113: 267-280.

https://doi.org/10.1016/0921-5093(89)90315-8.

[54] K. Tanaka, T. Mura. A dislocation model for fatigue crack initiation. J Appl Mech Mar 1981; 48: 97-103.

https://doi.org/10.1115/1.3157599.

[55] M. Lindroos, A. Laukkanen, T. Andersson, J. Vaara, A. Mäntylä, T. Frondelius. Micromechanical modeling of short crack nucleation and growth in high cycle fatigue of martensitic microstructures. Comp Mater Sci 2019; 170: 109185.

https://doi.org/10.1016/j.commatsci.2019.109185.

[56] H. Mughrabi, R. Wang. Cyclic stress-strain response and high-cycle fatigue behaviour of copper polycrystals. Mater Sci Monogr 1988; 46:1-13.

[57] R. Hill, The mathematical theory of plasticity. Oxford university Press 1998; 11.

[58] Y. Xu, W. Wan, F.P. Dunne. Microstructural fracture mechanics: Stored energy density at fatigue cracks. J Mech Phys Solids 2021; 146: 104209.

https://doi.org/10.1016/j.jmps.2020.104209.

[59] K. Sadananda, M. Nani Babu, A.K. Vasudevan. A review of fatigue crack growth resistance in the short crack growth regime. Mat Sci Eng A-Struct 2019; 754: 674-701.

https://doi.org/10.1016/j.msea.2019.03.102

[60] K. Sadananda, P. Shahinian. Prediction of threshold stress intensity for fatigue crack growth using a dislocation model. Int. J. Fract 1977; 13: 585–594.

https://doi.org/10.1007/BF00017294